Online Estimation of Battery Resistances in a Battery Integrated Modular Multilevel Converter

Lars Leister[1]*, Niklas Katzenburg[1], Phil Neugebauer[1] Lukas Stefanski[1] Marc Hiller[1]
1 Institute of Electrical Engineering, Karlsruhe Institute of Technology, Karlsruhe, Germany
*lars.leister@kit.edu

***Abstract*—For lifetime-optimized control of a modular multilevel converter battery energy storage system, determining the current state of health is crucial. Due to the degrees of freedom within the control of such a system, the utilization of dedicated test signals is possible without interrupting operation. In this paper, a method to determine internal battery resistance is described and implemented in the control structure of a prototype converter. The method is verified by measurement, and the results are validated by electrochemical impedance spectroscopy.**

***Index Terms*—Energy Storage System, Modular Multilevel Converter, Parameter Estimation, State of Health**

I. Introduction

Integrating batteries within the submodules of a cascaded H-bridge (CHB) or a modular multilevel converter (MMC) [1] as shown in Fig. 1a) allows the combination of batteries of different types or ages within one system [2]–[4]. Each power electronic storage block (PESB) contains a battery in parallel to its capacitor. As this setup comprises a battery energy storage system (BESS), such systems are often referred to as MMC-BESS. Due to the modular topology, the power flow can be controlled independently for each battery within the operational boundaries of the MMC. This allows for lifetime optimization of the batteries. The availability of the system also profits from its modularity. If a battery can or should no longer be used, it can be bypassed by the power electronics.

For the lifetime optimized operation, the condition of each battery in the system must be estimated. For instance, the estimation of state of health (SoH) can be done by Electrochemical Impedance Spectroscopy (EIS) under laboratory conditions, disrupting the operation of the system. To maintain the high availability of the system, an online SoH estimation method is proposed, using the available converter hardware to determine the internal battery resistance.

A. State of the Art

For reconfigurable batteries in a CHB topology, such methods have been discussed before, utilizing Kalman Filters (KFs) to estimate battery parameters [5]–[8]. These works focus on reducing the number of current and voltage sensors while utilizing load-induced current changes to create data for the KFs. While the required rapid load changes occur frequently

The project LeMoStore was funded by the Federal Ministry for Economic Affairs and Energy (BMWE) of Germany. The author is responsible for the content of this publication.

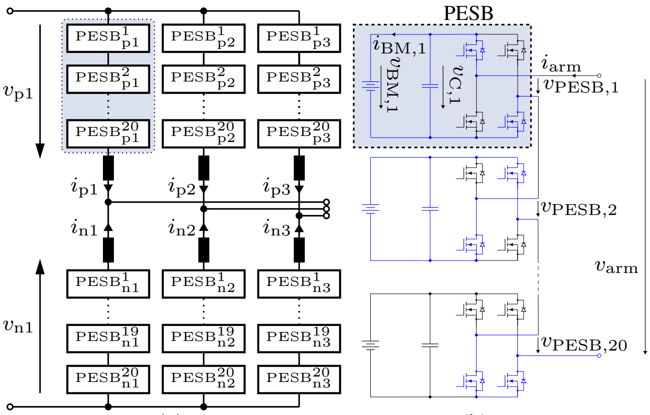

(a) (b)

Fig. 1. The MMC-BESS (a), one of its positive arms (b) with PESB_{p1}^{1} and PESB_{p1}^{2} in active states and PESB_{p1}^{20} in bypass.

in automotive applications, stationary BESS might operate under unchanged load conditions for extended time periods. In the works referenced above, the CHB is operated as a DC-supply, therefore constant modulation indices over multiple control periods are assumed. Due to this, the influence of a current controller as typically used in a grid-following MMC is not discussed. The current controller increases the estimation complexity due to its interaction with the modulation. Eliminating the battery voltage sensors also becomes more difficult as the current controller inherently counteracts the voltage drops induced by the current. However, the current sensors in the PESB can still be eliminated with the alternative method proposed in this paper, as discussed later in chapter VI.

In [9], another approach is shown to determine the battery capacity as an aging indicator. This is done by cycling and coulomb counting of individual battery modules during operation without disrupting the system's other functionalities. It is, however, time-consuming compared to the estimation of internal resistances. Both methods can be combined to increase the significance of the actual estimation of the SoH as discussed in chapter III.

B. Overview

In this paper, a method to determine the internal battery resistance without disrupting operation using dedicated test signals is proposed. The approach is mostly independent of the load profile and has a low computational complexity for the evaluation due to its well-defined test signals.

In the following chapters, the introduction of the hardware topology is followed by an overview of methods for the SoH estimation of batteries. After this, the embedding of the internal battery resistance estimation in the control structure of the MMC is shown. In chapter V, the execution of the estimation in hardware is verified, followed by the validation of the measurement results in chapter VI, proving the feasibility of the approach. The paper closes with its conclusion.

II. Hardware Topology

In the MMC-BESS, the PESB_{xy}^{z} are arranged in three phases $y \in \{1,2,3\}$, each divided in a positive and negative arm $x \in \{\mathrm{p,n}\}$. N PESB indexed $z \in \{1,2,...,N\}$ form one arm. This paper discusses a single arm of the MMC-BESS, as the arms are considered independent with respect to the estimation method. All variables are henceforth indexed only with $z \in \{1,2...N\}$ for clarity. The schematic of one arm is shown in Fig. 1b), where the three main states of the H-bridges are also shown: The two active states, where the battery module is part of the current path for both, while the output voltage sign differs, here shown as $v_{\mathrm{PESB},1} = +v_{\mathrm{BM},1}$ and $v_{\mathrm{PESB},2} = -v_{\mathrm{BM},2}$. One of the two bypass states is also shown with $v_{\mathrm{PESB},20} = 0\,\mathrm{V}$. It is crucial for the proposed method that redundant PESB are included in each of the arms. This is typically the case to achieve high availability. In the MMC arm used, three different battery types are used. An overview is later given in Tab. I. A detailed description of the prototype converter used can be found in [10].

III. State of Health Estimation

To characterize the age of a battery, the SoH is often considered in terms of Capacity-SoH ($\mathrm{SoH_C}$) and Resistance-SoH ($\mathrm{SoH_R}$). Both are important indicators and are not necessarily proportional to each other. The first one is defined as the ratio of the actual capacity C_{act} to the initial capacity C_0, i.e.,

$$SoH_{\mathrm{C}} = \frac{C_{\mathrm{act}}}{C_0}. \tag{1}$$

The latter is the focus of this paper and is defined dependent on the internal resistance's actual value $R_{\mathrm{i,act}}$, its initial value $R_{\mathrm{i,0}}$, and the End-of-Life (EOL) value $R_{\mathrm{i,EOL}}$ as

$$SoH_{\mathrm{R}} = \frac{R_{\mathrm{i,EOL}} - R_{\mathrm{i,act}}}{R_{\mathrm{i,EOL}} - R_{\mathrm{i,0}}}. \tag{2}$$

Application dependent, e.g., $R_{\mathrm{i,EOL}} = 2 \cdot R_{\mathrm{i,0}}$ is assumed. In fact, the battery impedance $\underline{Z}_{\mathrm{BM}}$ is not purely ohmic. A typical equivalent circuit model (ECM) capable of modeling transient behavior includes at least one or multiple RC-elements as shown in Fig. 2. While more precise electrochemical models exist, this model sufficiently illustrates the key factors. The total impedance comprises the RC-elements R_1, C_1 and R_2, C_2 as well as the ohmic resistance R_0. Additionally, the inductance L within the battery is often considered for the impedance, but not used as an aging indicator. The Warburg impedance $\underline{Z}_{\mathrm{W}}$ models the low frequency behavior of the battery cell. While it potentially can be used as an aging indicator, it is often neglected for practical reasons [11]. It should also be noted that the online estimation of the internal resistance is more limited in performance than an estimation in a laboratory with dedicated equipment and high effort. Overall it is therefore appropriate and sufficient to limit the estimation efforts to the 1RC and 2RC ECM.

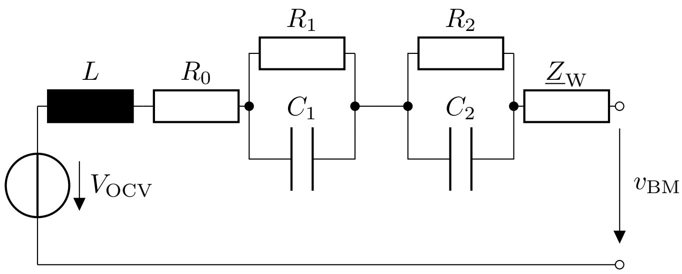

Fig. 2. Equivalent Circuit of a Battery.

The aforementioned R_i for SoH_{R} estimation is sometimes defined differently depending on the applied methodology. The purely ohmic resistance R_0 is often referred to as AC internal resistance (ACIR) as it can be measured at high frequencies or with very short pulses. The sum $R_0 + R_1(+R_2)$ is often referred to as DC internal resistance (DCIR) as it can be measured by applying low frequencies or long pulses [12]. Both can be considered as aging indicators [11]. They can be determined and differentiated by EIS and Hybrid Pulse Power Characterization (HPPC) as discussed in the following.

A. Electrochemical Impedance Spectroscopy

Galvanostatic EIS is carried out by supplying sinusoidal current at different frequencies f_{EIS} to a battery while measuring its voltage. The resulting complex impedance $\underline{Z}$ is commonly visualized as a Nyquist plot. Here, the expected impedance of the 14s22p battery modules mainly used in the prototype converter is considered. The plots in Fig. 3 are derived from a cell simulation model for *TerraE INR18650 30E* by BATEMO GmbH [13]. Additionally, the purely ohmic connection resistance of $10\,\mathrm{m\Omega}$ within the module was measured and is added in the plot. For different state of charge (SoC), one or two of the characteristic semicircles resulting from polarization and diffusion effects are visible, each roughly corresponding to one RC element in the ECM. The model does not include an inductance, therefore $\mathrm{Im}(\underline{Z}) \leq 0\,\Omega$. In the bottom part of the same figure, $|\underline{Z}|$ is shown over frequency, similar to a Bode plot. It is evident that different SoCs only affect the absolute resistance for frequencies below $200\,\mathrm{Hz}$.

The ACIR is typically considered at or around $1\,\mathrm{kHz}$ [12] while the DCIR is considered below $1\,\mathrm{Hz}$ [14]. During aging, when SoH decreases, the resistances increase, resulting in a widening of the semi-circles and an increase in the offset of the real part. EIS works best using high-quality sine waves and requires time to sweep through frequencies. In turn, it

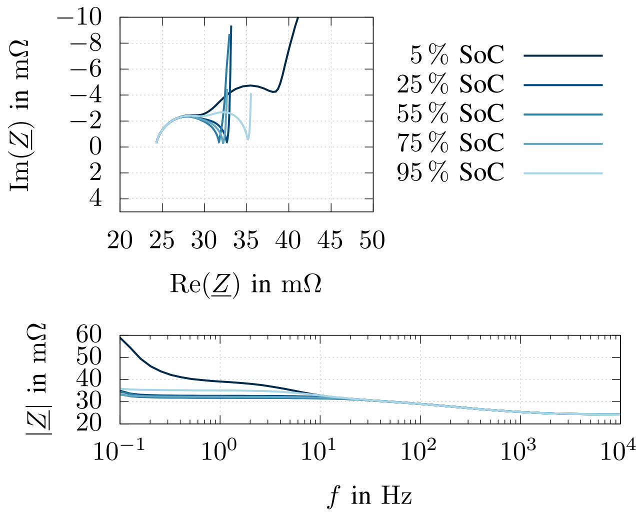

Fig. 3. Nyquist (top plot) and Amplitude (bottom plot) from simulation of the 14s22p battery module with the TerraE INR18650 30E cell model.

allows the differentiation of the real and imaginary parts of the impedance as a basis for parameter estimation. It is therefore often considered a benchmark regarding precise battery impedance estimation.

B. Hybrid Pulse Power Characterization

A faster alternative is the HPPC, where a sequence of current steps with a value of $I_{\mathrm{HPPC,ref}}$ is supplied to the battery, while the resulting voltage v_{BM} over the pulse duration $\Delta t_{\mathrm{p}} = t_1 - t_0$ is measured as shown in Fig. 4. This allows the estimation of the ACIR as

$$R_0 = \frac{\Delta V_0}{i_{\mathrm{BM}}(t_0)}. \quad (3)$$

A value close to the DCIR can also be determined by means of

$$R_0 + R_1 = \frac{\Delta V_0 + \Delta V_1}{i_{\mathrm{BM}}(t_1)} \quad (4)$$

dependent on the pulse duration Δt_{p}. By curve fitting, C_1 can also be estimated. The differentiation of the parameters requires sufficiently high time resolution compared to the time constant $\tau_{\mathrm{RC}} = R_1 \cdot C_1$ of the RC-element. The clear differentiation of the second RC element is even more difficult and often ambiguous. To compare the results of the HPPC and the EIS, parameter estimation as an intermediate step is a suitable approach.

When the 1RC ECM is used as a basis, the comparison via model comes down to [15]

$$R_{\mathrm{HPPC}}(8.24 \cdot t) \approx \mathrm{Re}\left(\underline{Z}_{\cdot \mathrm{EIS}}\left(t\right)\right). \quad (5)$$

This allows the transfer of EIS results to HPPC results. For example, the resistance determined by HPPC after 5 ms corresponds to the real part of the impedance determined by EIS at approximately 24 Hz. This allows the model-based validation of the results determined by HPPC with EIS data.

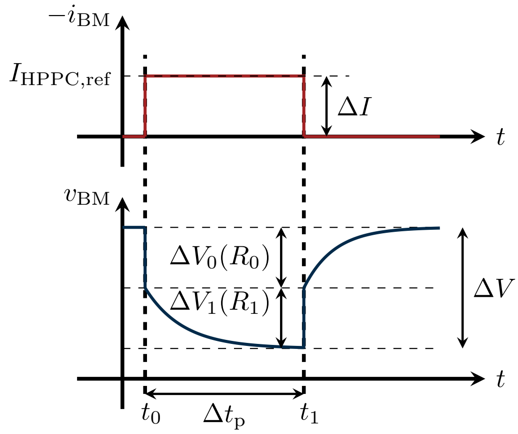

Fig. 4. HPPC and exemplary voltage response. Adapted from [14].

IV. MMC Integration

Due to the nature of the required current pulse, HPPC can be integrated into the arm control of the MMC-BESS. Coming from the general control structure, this will be shown next.

A. Control Structure

The control structure of the utilized MMC-BESS is centralized and cascaded [10]. The central control unit (CCU) is based on a system on a chip platform [16]. For each of the six arms, an arm control unit (ACU) based on a *MAX10* FPGA is in charge to control 20 local control units (LCUs). At the heart of each LCU is a microcontroller controlling both the switching of the H-bridge as well as the communication to the battery module's battery management system (BMS). In general, the setpoint voltage for each arm is determined by the current controller located on the CCU. Using a modulation similar to phase disposition pulse-width modulation (PWM), the ACU determines which PESB should be switched on completely and which PESB sets a voltage by PWM. The actual switching is handled by the LCUs which receive setpoint voltages from the ACU. The system runs at a control rate of 8 kHz. Due to the unipolar switching employed, the effective switching frequency of the PESB is 16 kHz. The voltage and the current of the battery modules are measured twice per 125 µs and are averaged. The ACU again averages these values over 2.5 ms (equaling 20 Samples at 8 kHz) and communicates them back to the CCU.

B. Adaptation for SoH Estimation

A signal-flow chart of the implementation to determine battery resistance during operation is shown in Fig. 5. The *Test Scheduler* on the CCU initiates the measurements for one battery module after another until all 20 battery modules within the arm are tested. It initiates a measurement for each battery module in PESB $h \in \{1,2...N\}$ by sending out the corresponding *TEST_ID*. It also ensures that a sufficiently high current i_{arm} is available to realize the targeted test current $I_{\mathrm{HPPC,ref}}$. When i_{arm} is an alternating current at 50 Hz, the peak current must be $\hat{i}_{\mathrm{arm}} > \sqrt{2} \cdot I_{\mathrm{HPPC,ref}}$ to achieve a 5 ms pulse duration. This is because the instantaneous current i_{BM} is never larger than i_{arm} except for transient interactions with the capacitor in the PESB. The test is postponed in case of a smaller arm current. The required test current and test type are transmitted with the variable *TEST_CMD*.

The HPPC starts with a relaxation period where $v_{\mathrm{PESB,ref},h} = 0\,\mathrm{V}$ and thus $i_{\mathrm{BM},h} = 0\,\mathrm{A}$. The arm voltage is set by the remaining PESB.

After the relaxation period of $5\,\mathrm{s}$, the test starts at the rising current edge of $|i_{\mathrm{arm}}|$ as soon as $|i_{\mathrm{arm}}| > I_{\mathrm{HPPC,ref}}$. For the following pulse period of $5\,\mathrm{ms}$, the *Selector* and *Feedforward* blocks calculate and send the required setpoint voltage $v_{\mathrm{PESB,ref},h}$ for the PESB under test every $8\,\mathrm{kHz}$ control cycle according to

$$v_{\mathrm{PESB,ref},h} = \frac{I_{\mathrm{HPPC,ref}}}{i_{\mathrm{arm}}} \cdot v_{\mathrm{C},h}. \qquad (6)$$

Hereby, $I_{\mathrm{HPPC,ref}}$ is the reference current for the HPPC and $v_{\mathrm{C},h}$ is the capacitor voltage of the PESB under test. The *Selector* block also sends the status of the current test back to the CCU. For the other submodules, a new reference arm voltage is calculated from the original arm reference voltage $v_{\mathrm{arm,ref}}$ by

$$v_{\mathrm{arm,rem,ref}} = v_{\mathrm{arm,ref}} - v_{\mathrm{PESB,ref},h}. \qquad (7)$$

Sorting is then executed normally without the PESB under test and the setpoints are sent to the remaining PESB (not shown in Fig. 5 for clarity). Due to the usage of H-bridges in the system, this approach is possible even for $v_{\mathrm{arm,ref}} = 0\,\mathrm{V}$ as opposing polarities between modules are possible.

The measurements $v_{\mathrm{BM},h}$ and $i_{\mathrm{BM},h}$ of the PESB under test are transferred via the ACU to the CCU with the maximum possible resolution of $\frac{1}{8\,\mathrm{kHz}} = 125\,\mathrm{\mu s}$. There, the *Test Interpreter* calculates the internal battery resistance. For this, the open circuit voltage V_{OCV} is averaged over at least 8 Samples during relaxation. After this, $v_{\mathrm{BM},h}$ and $i_{\mathrm{BM},h}$ are averaged over 41 Samples after the current i_{BM} is within $\pm 1\,\mathrm{A}$ of $I_{\mathrm{HPPC,ref}}$. This equals $5\,\mathrm{ms}$. Values during the rise of i_{BM} are disregarded as they are not considered representative. Naturally and even more due to the averaging, the resulting internal resistance R_{HPPC} contains parts from both R_0 and R_1.

C. Error Propagation

In preparation for the practical application within the MMC-BESS, the attainable quality of the results is determined. The voltage measurement on the LCU is done by the 12 bit analog-to-digital converter (ADC) of the microcontroller *TMS320F280025*. Assuming $\Delta V = 0.4\,\mathrm{V}$ and considering the voltage divider of $560\,\mathrm{k\Omega}$ and $30\,\mathrm{k\Omega}$ this gives $\Delta V_{\mathrm{ADC}} = 20\,\mathrm{mV}$. With the reference voltage $V_{\mathrm{ref,ADC}} = 3.3\,\mathrm{V}$, the quantization step size of the ADC is $\Delta V_{\mathrm{ADC}} \approx 0.8\,\mathrm{mV}$. Given the differential nonlinearity of the ADC of $\pm 0.5\,\mathrm{LSB}$, this results in a maximum error of the voltage difference measurement $g_{\mathrm{v}} = \pm\frac{0.4\,\mathrm{mV}}{20\,\mathrm{mV}} = \pm 2\,\%$. The resistor tolerances in the voltage divider barely influence the results, as the absolute voltage is not relevant.

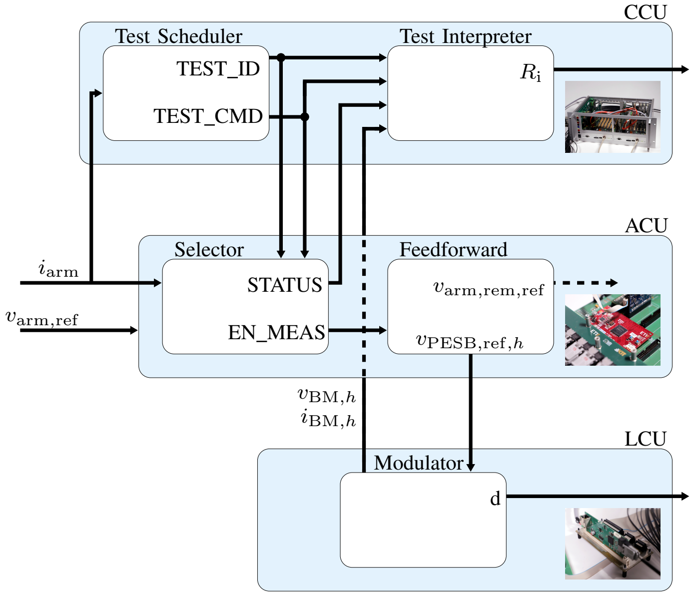

Fig. 5. Signal flow chart of the online battery test signal generation.

The current is measured by a *LEM HXS 20-NP* hall sensor with an accuracy of $\pm 1\,\%$ and a linearity error of $\pm 0.5\,\%$ of the nominal current $I_{\mathrm{PN}} = 20\,\mathrm{A}$. For an assumed HPPC current below I_{PN}, this gives a maximum error for the current measurement of $g_{\mathrm{i}} = \pm 1.5\,\%$.

The total error for R_{i} is then given as roughly $g_{\mathrm{R}} = g_{\mathrm{v}} + g_{\mathrm{i}} = \pm 3.5\,\%$. For a resistance in the range of $40\,\mathrm{m\Omega}$ this means a deviation of up to $\pm 1.4\,\mathrm{m\Omega}$. It should be noted that quantization errors and other factors that potentially increase the total error are neglected.

V. Application

For this paper, the MMC is connected to an *EGSTON* grid emulator supplying an ideal three phase $400\,\mathrm{V}$, $50\,\mathrm{Hz}$ grid. The common DC voltage of the MMC is set to $0\,\mathrm{V}$, therefore the DC power $P_{\mathrm{DC}} = 0\,\mathrm{W}$. This is done due to a lack of availability of an appropriate DC source and does not impact the universal applicability of the shown approach. Within the PESB, 14s22p battery modules are included. The battery cell types and their states before this measurement are shown in Tab. I.

A mixture of different battery cells is used, which are also at different SoCs. All modules are new, i.e., have an SoH close to $100\,\%$. The measurement is executed during operation in a steady state at $\hat{i}_{\mathrm{arm}} = 15\,\mathrm{A}$ and $I_{\mathrm{HPPC,ref}} = 10\,\mathrm{A}$. The arm current amplitude must be large enough to provide a current above $I_{\mathrm{HPPC,ref}}$ for at least the desired pulse duration. Higher arm currents are also compatible with the parameter estimation and merely result in an extension of the possible pulse duration. In addition, internal currents can be driven within the converter to increase the arm current if sufficient AC current is not available.

TABLE I
BATTERIES USED WITHIN THE ARM (EIGHT HIGHEST SOC MARKED RED)

PESB	Cell	SoC
1	LGChem 18650 M29	76 %
2	LGChem 18650 M29	55 %
3	LGChem 18650 M29	56 %
4	TerraE 18650 30E	54 %
5	DMEGC 18650 29E	43 %
6	DMEGC 18650 29E	62 %
7	DMEGC 18650 29E	41 %
8	DMEGC 18650 29E	39 %
9	TerraE 18650 30E	43 %
10	TerraE 18650 30E	65 %
11	TerraE 18650 30E	46 %
12	TerraE 18650 30E	67 %
13	TerraE 18650 30E	45 %
14	TerraE 18650 30E	68 %
15	TerraE 18650 30E	47 %
16	TerraE 18650 30E	71 %
17	TerraE 18650 30E	51 %
18	TerraE 18650 30E	73 %
19	TerraE 18650 30E	56 %
20	TerraE 18650 30E	53 %

A. *Methodology*

To validate the online capability of the implementation, an *HBK Gen7tA* synchronized with a *HBK Gen4tB* is used [17]. With this measurement setup, not only the arm voltage v_{arm} and current i_{arm}, but also the 20 battery currents i_{BM} and the 20 PESB output voltages v_{PESB} are captured simultaneously and with a sample rate of 2 MS/s. For the operation, a maximum of eight PESB is switched on simultaneously, including the PESB under test. As the test is executed during discharge operation of the system, the eight batteries with the highest SoC are highlighted in Tab. I as those will be used in operation due to active balancing within the arm.

B. *Online capability*

In Fig. 6, the measured data during two grid cycles are shown. In the second half of the first shown cycle, the online impedance measurement for PESB 1 is executed. The measurement is done during negative arm power, i.e., during discharge. However, the characterization is done with a charge pulse in this case. From Fig. 6b), this is evident. The current $i_{\text{BM},1}$ is positive during the second half wave of the first period and close to the target current of $I_{\text{HPPC,ref}} = 10\,\text{A}$. Before this, the PESB 1 was not used to ensure relaxation times. From the switching behavior in Fig. 6c) and even better in the close up in Fig. 6d) it is clear that PESB 3 is used to counteract the voltage of PESB 1. As a result, current control and general normal operation are not influenced, which is shown by the continuously sinusoidal arm current waveform in Fig. 6a). After the characterization of PESB 1 is finished, the module continues normal operation as it is rather highly charged and is therefore prioritized by the sorting algorithm. This is also the reason for the change of the depicted voltage waveform in Fig. 6a): Before and during characterization of PESB 1, a module with lower voltage must compensate for its omission. Due to the lower voltage, one module is not

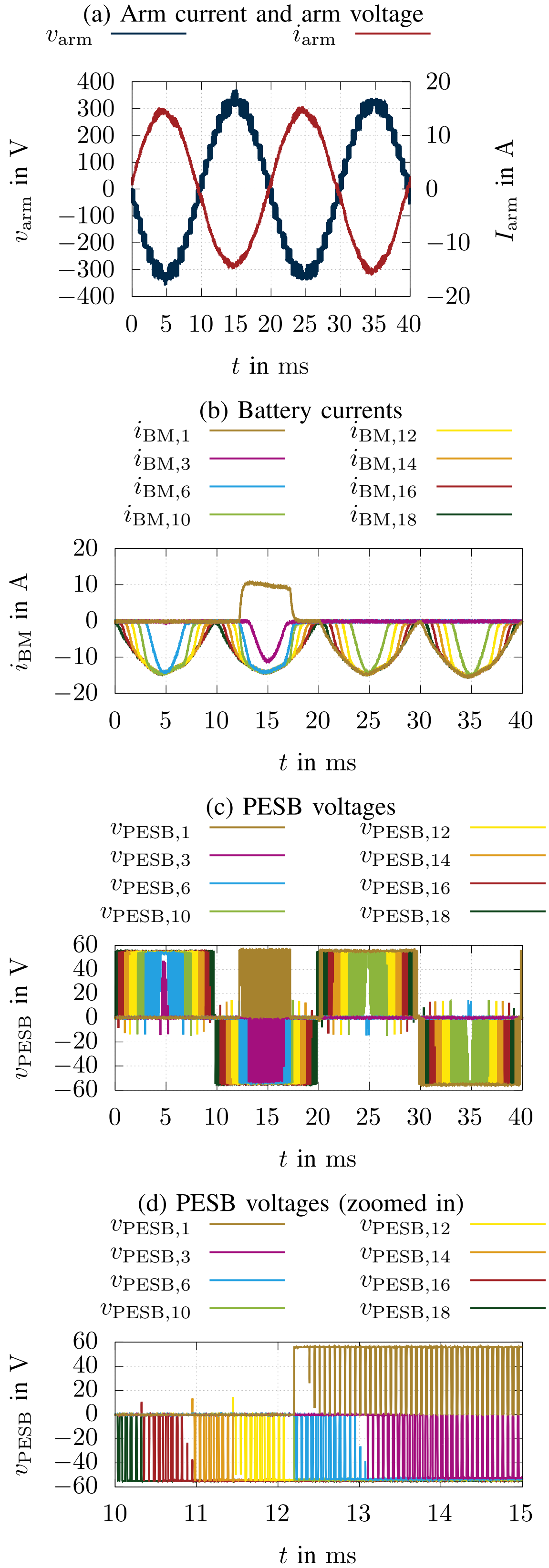

Fig. 6. Measured voltages and currents during online resistance estimation in operation.

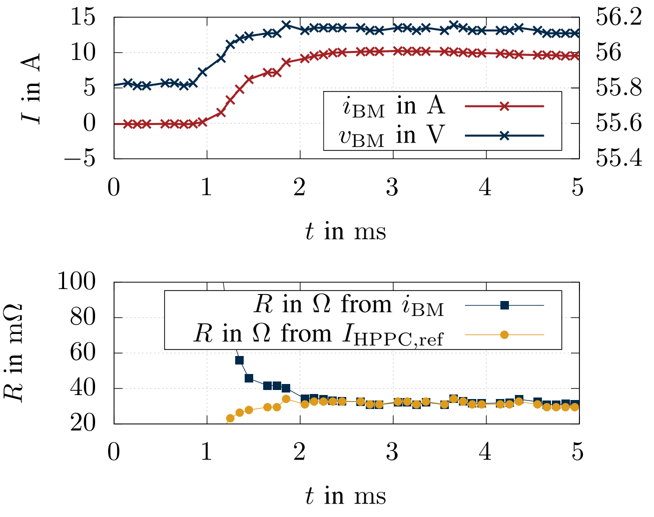

Fig. 7. Resistance calculation during online estimation.

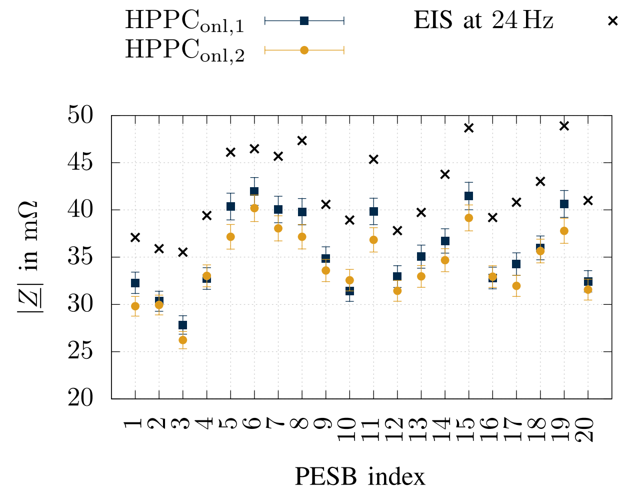

Fig. 8. Repeated online resistance measurement.

sufficient, so another module must be switched on. This results in the higher peak voltage v_{arm} during characterization due to PWM. The current control of the tested PESB is shown to work as intended. The total voltage of the arm, averaged over the PWM period of 8 kHz, is unaltered due to the seamless exchange with another PESB.

VI. Results

During the parameter estimation for PESB 1, the PESB itself measures the data shown in Fig. 7 and sends it via ACU to the CCU. The measured battery voltage v_{BM} begins to rise before the measured battery current i_{BM}. This is mainly caused by the additional measurement delay by the current transducer and the location of the voltage measurement rather close to the capacitor voltage measurement on the PESB PCB. In the lower plot, the resistance value is calculated: In blue, the current measured by the PESB is used for the calculation, while in orange, the resistance calculated from the setpoint current $I_{hppc,ref}$ is used. Clearly, the calculated values converge. Therefore, the method does not necessarily require dedicated battery current sensors. It is sufficient to measure the arm current and determine the PESB duty cycle accordingly. However, it must still be ensured that the resistance is only calculated once the current is actually flowing in the battery.

A. Online SoH Measurement

In Fig. 8, the resulting internal resistances for all 20 PESBs are shown. To demonstrate the reproducibility, the test was carried out twice, two days apart, with the batteries resting in between. The results from the two measurements are close to each other, with the highest deviation being roughly $3\,\mathrm{m\Omega}$. The error bars shown represent $g_R = \pm 3.5\,\%$ as derived in section IV-C. For most modules, the two measurement results lie within each other's error range. The differences between the battery modules are greater, which implies larger differences even between supposedly identical batteries than expected. For example, the battery module from PESB 15 gives roughly $R_{HPPC,BM,15} \approx 41\,\Omega$ in the first online HPPC measurement, while the PESB 20 gives roughly $R_{HPPC,BM,20} \approx 32\,\Omega$ in the same measurement run. This discrepancy between those batteries is higher than expected, given that the modules in PESB 15 and PESB 20 have the same battery cells and roughly the same SoC with 47 % and 53 %, respectively. Additionally, the values are higher than expected from the simulation as shown in Fig. 3. The reason for this is investigated in the following section VII.

VII. Discussion and Impedance Reference

The differences between modules determined by online HPPC are verified by EIS characterization. The measurement is executed with a *Gamry Interface 1010E* combined with an *NF BN4610* power supply. The four-wire connection is wired to the PESB, close to the internal battery voltage measurement. This ensures consistent results in comparison to the online HPPC measurements. The battery modules from PESB 15 and PESB 20 are chosen for a detailed comparison as their impedances in the online HPPC results largely differ. The SoC is kept at the same value, i.e., the batteries were neither charged nor discharged between the online HPPC and EIS. In Fig. 9, the results are shown. Similarly to the simulation results in Fig. 3, the Nyquist plot for both modules is shown at the top, while the absolute value of $\underline{Z}$ is shown in the bottom part. The EIS measurement confirms that the impedances of these modules do indeed differ. This is assumed to be related to a longer storage period of the battery modules in the order of magnitude of one year before the tests shown here were executed. Additionally, the operation time of the system was very limited, resulting in the battery modules not being fully cycled. The electrochemical reasons are not investigated here. However, the passive anode effect might play a role [18].

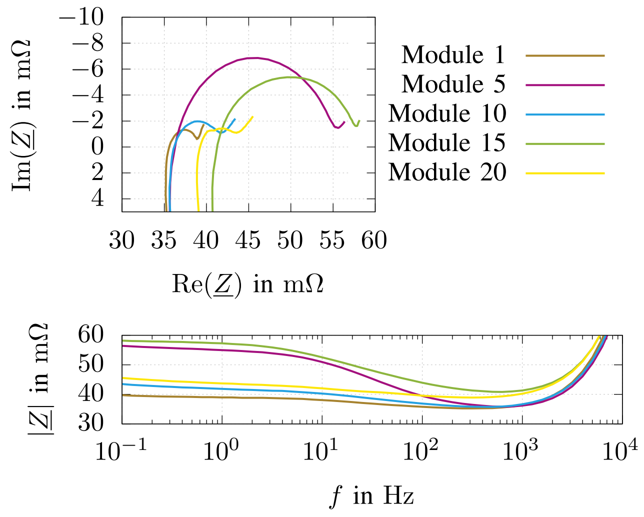

Fig. 9. Nyquist (top plot) and Amplitude (bottom plot) measured for two batteries.

A. Comparison of Online Estimation and EIS

The impedance determined by EIS can now be compared to the results from HPPC according to [15]. Therefore, Fig. 8 includes the absolute value of the impedance from EIS at 24 Hz. This neglects the fact that the online determined values are averaged over all valid samples, as this only corresponds to the resistance calculated 5 ms after pulse start. However, only the relative values between batteries are relevant and are consistent throughout online estimation and EIS.

VIII. Conclusion

The approach to determine the internal battery resistance of batteries in an MMC-BESS has proven to be feasible. It can be successfully executed during the operation of the converter. The method is effective, demonstrating unexpected differences between the battery modules in the prototype converter. It has been shown by EIS reference measurements that the measured differences are not a result of measurement errors but are rooted within the batteries' electrochemistry.

The capability of the system to determine the actual internal resistance of the battery modules during operation within seconds enables the lifetime-optimized operation of the system as a whole. The demonstrated reproducibility of the online estimation is key for this, as it ensures the traceability of the resistance over time. With this, the way to SoH_R tracking during the converter lifetime is paved. Nevertheless, the achievable performance of the SoH estimation must be further investigated by lifetime testing.

Acknowledgment

The authors acknowledge that the battery cell simulation model used in this paper was provided by Batemo GmbH for the LeMoStore project. Furthermore, the Gen4tB power analyzer was provided by Hottinger Brüel & Kjaer GmbH for the LeMoStore project, too.

References

[1] R. Marquardt, A. Lesnicar, and J. Hildinger, “Modulares Stromrichterkonzept für Netzkupplungsanwendungen bei hohen Spannungen,” in *ETG-Fachtagung*, Bad Nauheim, Germany, 2002.

[2] M. Schroeder, S. Henninger, J. Jaeger, A. Raš, H. Rubenbauer, and H. Leu, “Integration of batteries into a modular multilevel converter,” in *2013 15th European Conference on Power Electronics and Applications (EPE)*, Sep. 2013, pp. 1–12.

[3] A. Hillers, M. Stojadinovic, and J. Biela, “Systematic comparison of modular multilevel converter topologies for battery energy storage systems based on split batteries,” in *2015 17th European Conference on Power Electronics and Applications (EPE'15 ECCE-Europe)*, Sep. 2015, pp. 1–9.

[4] M. Gommeringer, F. Kammerer, J. Kolb, and M. Braun, “Novel DC-AC Converter Topology for Multilevel Battery Energy Storage Systems,” *PCIM Europe : International Exhibition and Conference for Power Electronics, Intelligent Motion, Renewable Energy and Energy Management, Nuremberg, 14 - 16 May 2013 ; proceedings*, p. 699, 2013.

[5] N. Tashakor, F. Naseri, J. Fang, A. H. Zadeh, and S. Goetz, “Module Voltage and Resistance Estimation of Battery-Integrated Cascaded Converters through Output Sensors Only for EV Applications,” *IEEE Transactions on Transportation Electrification*, pp. 1–1, 2023.

[6] N. Tashakor, B. Arabsalmanabadi, F. Naseri, and S. Goetz, “Low-Cost Parameter Estimation Approach for Modular Converters and Reconfigurable Battery Systems Using Dual Kalman Filter,” *IEEE Transactions on Power Electronics*, vol. 37, no. 6, pp. 6323–6334, Jun. 2022.

[7] N. Tashakor, F. Naseri, J. Fang, H. Schotten, and S. Goetz, “Voltage and Resistance Estimation of Battery-Integrated Cascaded Converters,” in *IECON 2022 – 48th Annual Conference of the IEEE Industrial Electronics Society*, Oct. 2022, pp. 1–6.

[8] N. Tashakor, B. Arabsalmanabadi, E. Hosseini, K. Al-Haddad, and S. Goetz, “Estimation of Battery Parameters in Cascaded Half-Bridge Converters with Reduced Voltage Sensors,” in *2022 24th European Conference on Power Electronics and Applications (EPE'22 ECCE Europe)*, Sep. 2022, pp. 1–11.

[9] Z. Ma, F. Gao, X. Gu, N. Li, and D. Niu, “An Online SOH Testing Method of MMC Battery Energy Storage System,” in *2018 IEEE 19th Workshop on Control and Modeling for Power Electronics (COMPEL)*, Jun. 2018, pp. 1–7.

[10] N. Katzenburg, K. Kuhlmann, L. Leister, L. Stefanski, J. Teigelkötter, and M. Hiller, “Design of a Modular Multilevel Converter with 400 kWh of Integrated Batteries,” in *2023 22nd International Symposium on Power Electronics (Ee)*. Novi Sad, Serbia: IEEE, Oct. 2023, pp. 1–8.

[11] P. Iurilli, C. Brivio, and V. Wood, “On the use of electrochemical impedance spectroscopy to characterize and model the aging phenomena of lithium-ion batteries: A critical review,” *Journal of Power Sources*, vol. 505, p. 229860, Sep. 2021.

[12] A. Narusawa, “From 1 hour to Just 10 Seconds: Using the Low-frequency AC-IR Method as a Quicker and More Stable Alternative to DC-IR Testing of Lithium Ion Batteries,” May 2015.

[13] “INR18650-30E,” https://www.batemo.com/de/products/batemo-cell-explorer/terrae-inr18650-30e/.

[14] W. Waag, S. Käbitz, and D. U. Sauer, “Experimental investigation of the lithium-ion battery impedance characteristic at various conditions and aging states and its influence on the application,” *Applied Energy*, vol. 102, pp. 885–897, Feb. 2013.

[15] L. Leister, D. Schall, N. Katzenburg, L. Geier, L. Stefanski, and M. Hiller, “Mutual Transferability of the Results From HPPC and EIS for Internal Battery Resistance Estimation,” in *PCIM Conference 2026*, Jun. 2026.

[16] B. Schmitz-Rode, L. Stefanski, R. Schwendemann, S. Decker, S. Mersche, P. Kiehnle, P. Himmelmann, A. Liske, and M. Hiller, “A modular signal processing platform for grid and motor control, HIL and PHIL applications,” in *2022 International Conference on Power Electronics and ECCE Asia (IPEC-Himeji 2022 -ECCE Asia)*, 2022.

[17] N. Katzenburg, L. Leister, A. Stock, L. Stefanski, and M. Hiller, “In-Depth Analysis of Multilevel Battery Systems with Multi-Channel High-Performance Data Acquisition,” in *PCIM Conference 2026*, Jun. 2026.

[18] A. Krupp, R. Beckmann, T. Diekmann, E. Ferg, F. Schuldt, and C. Agert, “Calendar aging model for lithium-ion batteries considering the influence of cell characterization,” *Journal of Energy Storage*, vol. 45, p. 103506, Jan. 2022.